Paleoceanography and Paleoclimatology

RESEARCH ARTICLE
10.1029/2021PA004229

Late Oligocene Precipitation Seasonality in East Asia Based on $\delta^{13}C$ Profiles in Fossil Wood

J. R. Vornlocher[1,2], W. E. Lukens[3], B. A. Schubert[1], and C. Quan[4]

[1]School of Geosciences, University of Louisiana at Lafayette, Lafayette, LA, USA, [2]Department of Geology and Environmental Science, University of Pittsburgh, Pittsburgh, PA, USA, [3]Department of Geology and Environmental Science, James Madison University, Harrisonburg, VA, USA, [4]School of Earth Science and Resources, Chang'an University, Xi'an, China

Key Points:

- A seasonal rainfall proxy using tree ring $\delta^{13}C$ profiles was validated using living trees and weather station records in southern China
- Late Oligocene fossil tree ring $\delta^{13}C$ variations were consistent with rainfall levels ~4.5X higher in summer than winter
- Results suggest evidence for an East Asian Monsoon-style system in the Late Oligocene

Supporting Information:

Supporting Information may be found in the online version of this article.

Correspondence to:

W. E. Lukens,
lukenswe@jmu.edu

Citation:

Vornlocher, J. R., Lukens, W. E., Schubert, B. A., & Quan, C. (2021). Late Oligocene precipitation seasonality in East Asia based on $\delta^{13}C$ profiles in fossil wood. *Paleoceanography and Paleoclimatology*, *36*, e2021PA004229. https://doi.org/10.1029/2021PA004229

Received 20 JAN 2021
Accepted 21 MAR 2021

Abstract The onset, characteristics, and drivers of paleo-monsoon conditions in East Asia remain a topic of heated debate. Records from the Eocene suggest pronounced rainfall seasonality consistent with monsoon rainfall across China, likely driven by migrations of the Inter-Tropical Convergence Zone. Model simulations indicate that modern-like monsoon circulation of China was established by the early Miocene at the latest, but uncertainty remains due to a paucity of proxy records from the Oligocene. Here, we provide the first annually resolved, quantitative estimates of seasonal precipitation from East Asia during the Oligocene, based upon intra-annual variation in carbon isotopes across growth rings of exquisitely preserved fossil wood from southern China. We find a clear pattern of consistent, summer-dominated precipitation with ~4.5 times more precipitation in summer (P_s) than winter (P_w). Seasonal precipitation estimates were calculated using Monte Carlo resampling, resulting in median P_s = 1,042 (95% C.I. = 628–1,517) and P_w = 235 (95% C.I. = 50–578), which are indistinguishable from the instrument record at a nearby weather station, where P_s = 977 (95% C.I. = 662–1,434) and P_w = 292 (95% C.I. = 165–515), and from proxy application on two modern trees near the fossil site, where P_s = 1,058 (95% C.I. = 617–1,558) and P_w = 188 (95% C.I. = 31–583). These data demonstrate that by the late Oligocene, precipitation patterns in East Asia had similar strength and seasonality to modern conditions, which suggests the presence of an East Asian Monsoon-style system prior to the Neogene.

Plain Language Summary Prediction of monsoon behavior under warming climate conditions can be aided by studies of monsoon dynamics from ancient warm intervals, such as the late Oligocene (~25 million years ago). We applied a novel technique to reconstruct rainfall patterns in southern China using high-resolution stable carbon isotope profiles in incredibly well preserved fossil wood. To demonstrate the robustness of this approach, we first tested the method using living trees and a nearby weather station. We then applied this method to fossil wood from the late Oligocene. Our results suggest that summer rainfall (May–October) was ~4 times more than winter rainfall (November–April), which is indistinguishable from modern conditions in southern China. We conclude that the East Asian monsoon system was as strong as it is today during its very early stages in the Oligocene.

1. Introduction

The Cenozoic evolution of Asian monsoon systems remains a rich topic of debate and active, interdisciplinary investigation. Paleoclimate proxies and simulations suggest that highly seasonal precipitation existed across southern Asia in the Eocene, likely driven by migrations of the Inter-Tropical Convergence Zone similar to the modern South Asian Monsoon or Indonesian-Australian Monsoon systems (Farnsworth et al., 2019; Li et al., 2018; Spicer et al., 2016; Tardif et al., 2020). A key feature of this early to middle Paleogene climate pattern is a west-east arid belt spanning much of China (Sun & Wang, 2005) that was possibly driven by the presence of a persistent high pressure system over central Asia (Tardif et al., 2020). This pattern differs from the modern East Asian Monsoon (EAM), which involves an incursion of moist air that penetrates deep into China and therefore disrupts a zonal precipitation gradient (Wang & LinHo, 2002). The timing of EAM initiation remains debated, ranging from the Eocene (Quan et al., 2012; Xie et al., 2019) to the late Oligocene (Sun & Wang, 2005) and Miocene (Clift et al., 2008; Farnsworth et al., 2019; Liu et al., 2017; Spicer et al., 2017). We contend that a key driver of this disagreement arises from a paucity of proxy records from East Asia during the Oligocene, compared to the Eocene and Miocene.

Precipitation seasonality and variability are intrinsic to monsoon systems; however, the majority of paleoclimate proxies applied to paleo-monsoon systems reconstruct mean annual conditions averaged across long timescales (decades to 10^5 years), large geographic areas, or offer qualitative interpretations of monsoon strength and pattern. The presence and characteristics of paleo-monsoons have been inferred indirectly through sedimentology (Licht et al., 2014; Loope et al., 2001), the stable isotope composition of paleosols (Passey et al., 2009; Quade et al., 1989; Suarez et al., 2011; Zhisheng et al., 2005), soil and rock magnetics (Liu et al., 2007; Yancheva et al., 2007), cosmogenic radionuclides (Beck et al., 2018), and paleobotanical proxies (Quan et al., 2012; Spicer et al., 2017; Spicer et al., 2016; Xie et al., 2019, 2020). High-resolution isotope analysis on corals (Aggarwal et al., 2004; Su et al., 2010), speleothems (Cheng et al., 2016; Fleitmann et al., 2003; Kathayat et al., 2017), gastropods (Licht et al., 2014), and mammal tooth enamel (Licht et al., 2014) can record intra- to inter-annual paleoclimate patterns. However, coral and speleothem records are only available for the Quaternary Period, and quantitative models for annual isotope variations in shells or teeth are not widely applied in deep-time (though see Passey et al., 2005; Yang et al., 2020). Recent schlerochronological analyses from Paratethys Sea oysters coupled with numerical model simulations have provided some of the first high resolution, seasonal paleoclimate reconstructions from the Eocene of central Asia and support interpretations of strongly seasonal precipitation over the region prior to the Neogene (Bougeois et al., 2014, 2018). While these marine paleoclimate proxies offer a substantial contribution to understanding the seasonal paleoclimatology of Asian monsoons, new terrestrial proxy records are needed for the Oligocene due to the closure of the Paratethys Sea at the end of the Eocene (van der Boon et al., 2018).

Here, we present an annually resolved, quantitative reconstruction of summer and winter monsoon precipitation from southern China during the late Oligocene using stable carbon isotope measurements across growth rings of exquisitely preserved fossil wood, thus producing the first annual record of seasonal precipitation in East Asia from deep time. The late Oligocene Epoch of the Paleogene Period is an ideal time period for studying monsoon strength and variability because it post-dates major central Tibetan uplift (Fang et al., 2020) and coincides with the last time that CO_2 levels were consistently at least as high as today (Cui et al., 2020; Foster et al., 2017); however, paleoprecipitation records from the Oligocene in East Asia are rare. This new paleoclimate record fills a key gap in proxy records from a region where billions of people rely on accurate forecasts of current and future monsoon dynamics.

2. Materials and Methods

2.1. Fossil and Living Trees

Three fossil wood specimens were selected for analysis from the Santang Konservat Lagerstätte, a newly described fossil plant assemblage (Huang et al., 2018; Quan et al., 2016; Ying et al., 2018). The taxonomic affinity of these fossils have been described previously by Huang et al. (2018), who observed traits in fossil specimens to be consistent with *Castanopsis sp*., a genus in the Fagaceae family with evergreen habit that lives today in tropical to subtropical East and Southeast Asia. Wood specimens of the fossil assemblage are stored and fully accessible in the Biological Museum of Sun Yat-sen University, Guangzhou, China.

The Santang fossil assemblage is preserved within a single lacustrine deposit of the upper Yongning Formation in Nanning Basin, Guangxi, China (22.881°N, 108.417°E, elevation = 83 m) (Figures 1a and 1b) (Quan et al., 2016). The site is dated to late Oligocene based on *Anthracotherium changlingensis*, *Anthracokeryx kwangsiensis*, and *Heothema* mammal fossil assemblages within the upper Yongning Formation (Ying et al., 2018; Zhao, 1993), and independently supported by palynofloral analysis (Wang et al., 2015). Three fossil wood samples (NNW010, NNW12B, and NNW021, Figures 1f–1h) were selected for intra-ring $\delta^{13}C$ analysis in this study. Each ring was subdivided by hand using a razor blade perpendicular to the growth axis (Schubert & Jahren, 2011). A total of 20 rings were sampled (n = 518 slices), with an average of 25 samples (range = 12–43) per growth ring.

We also studied two radial cores of evergreen trees living nearby the fossil assemblage (*Pinus massoniana*; samples QXS21A and QXS24A, Figures 1d and 1e). Tree cores were extracted with an increment borer in 2016 at Qingxiushan Hill, Nanning, Guangxi, China (22.790°N, 108.384°E, elevation = 223 m, Figure 1b). These trees were selected to test the seasonal precipitation proxy on extant evergreen trees growing in a monsoon-affected climate (Figure 1c). Consecutive growth rings spanning the years 1990–2000 were

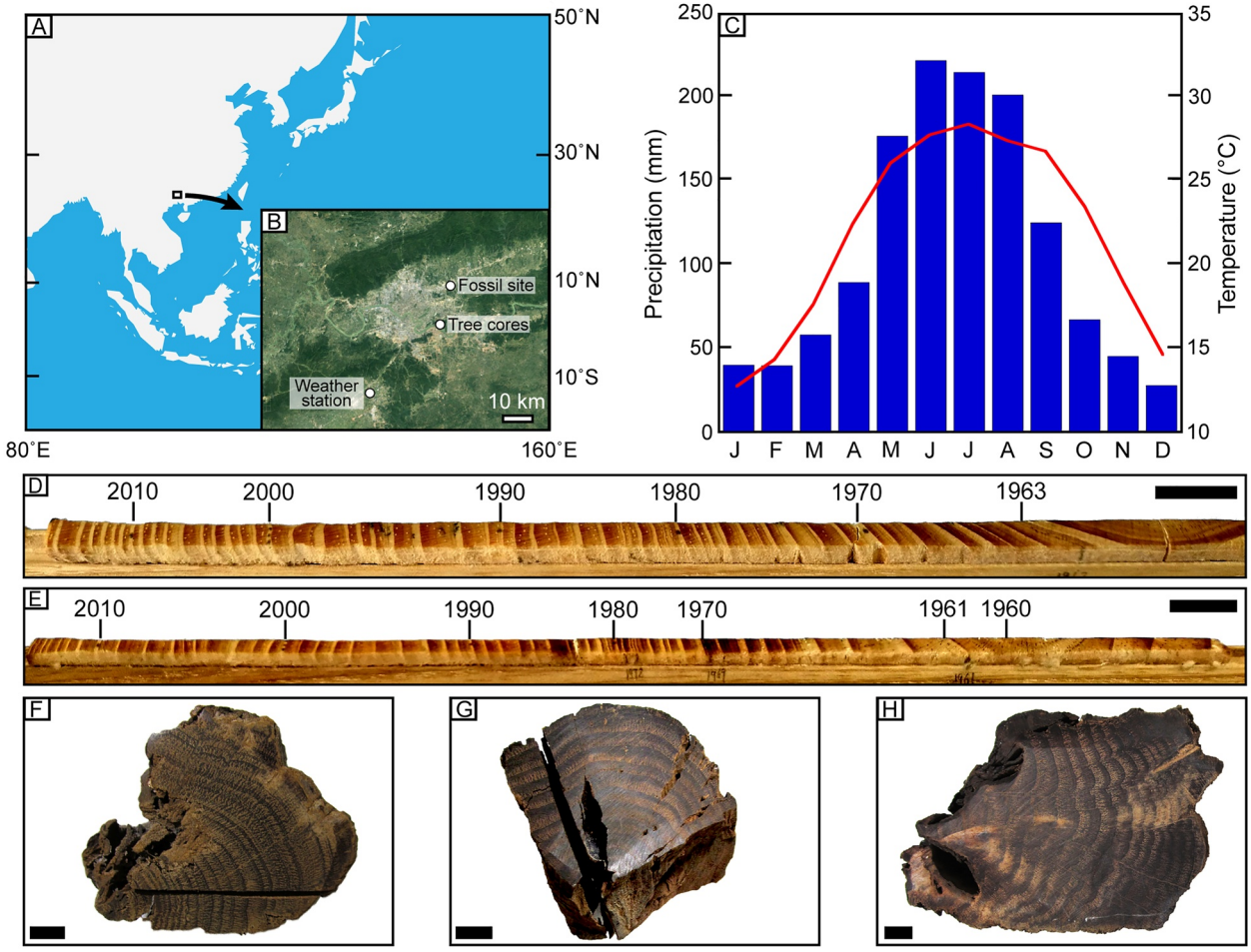

Figure 1. (a) Location map and samples collected within the Nanning Basin, southern China. (b) Locations of the modern tree cores, the local weather station (China Meteorological Data Service Center, Station No. 59431, http://data.cma.cn/), and fossil trees at the Santang Konservat Lagerstätte. Imagery courtesy of USGS/NASA Landsat via Google Earth. (c) Average monthly precipitation (blue bars) and temperature (red line) for Nanning, China (1951–2016 CE). (d and e) Photographs of the modern *Pinus massoniana* tree cores QXS21A (top) and QXS24A (bottom). Growth direction is to the left. Years are labeled for reference. (f–h) Photographs of the fossil evergreen wood samples used for this study: (f) NNW010, (g) NNW12B, and (h) NNW021. For each wood sample, earlywood occurs as light bands and latewood occurs as subsequent dark bands. All black scale bars = 1 cm.

sampled in an identical manner to the fossil wood. A total of 317 slices were collected from the two cores, with an average of 14 samples (range = 8–12) per growth ring.

2.2. Stable Isotopes and Data Analysis

For modern and fossil samples, bulk wood slices weighing between 80 and 150 μg were wrapped in tin capsules for $\delta^{13}C$ analysis. Cellulose was not extracted for these data; previous work has shown a robust linear correlation between the $\delta^{13}C$ value recorded in bulk wood tissue and α-cellulose (Lukens et al., 2019a), and the goal of the current study was to analyze relative changes in $\delta^{13}C$ value rather than exact values (after Schubert & Jahren, 2011). All $\delta^{13}C$ values were determined using a Thermo Finnigan Elemental Analyzer (Flash EA 1112 Series) coupled with a Delta V Advantage isotope-ratio mass spectrometer (Thermo Fisher) at the University of Louisiana at Lafayette. Samples were analyzed with three internal laboratory reference materials (JGLY, $\delta^{13}C = -43.51‰$; JHIST, $\delta^{13}C = -8.13‰$; JGLUC, $\delta^{13}C = -10.52‰$). A quality assurance sample (JRICE, $\delta^{13}C = -27.44‰$) was analyzed as an unknown with each batch run, and yielded a <0.1‰ analytical uncertainty. Isotope values are reported in δ-notation (‰) with respect to Vienna Pee Dee Belemnite.

All analyses of meteorological and $\delta^{13}C$ data were performed in RStudio version 3.6.1 (R Core Team, 2020).

2.3. Seasonal Precipitation Proxy

We reconstructed the ratio of seasonal, 6-month summer (P_s: May through October) and winter (P_w: November through April) precipitation in the Nanning Basin by applying a proxy system model (cf., Evans et al., 2013) developed by Schubert and Jahren (2011) to the intra-ring $\delta^{13}C$ analyses from modern and Oligocene trees. This proxy was calibrated using a global data set of intra-ring $\delta^{13}C$ records from 33 angiosperm and gymnosperm trees growing across a range of environments (15 total sites), including southeast Asia. We note that other modern and fossil applications of this seasonal precipitation proxy have confirmed its utility for reconstructing seasonal rainfall across a wide latitudinal range (tropic to polar regions) and low or high seasonality (Judd et al., 2019; Schubert & Timmermann, 2015; Schubert et al., 2012, 2017).

The proxy relates the amplitude of $\delta^{13}C$ values within a ring (H; maximum $\delta^{13}C$ minus the preceding minimum $\delta^{13}C$ value) to the annual variation in $\delta^{13}C$ of atmospheric CO_2 [$\Delta(\delta^{13}C_{CO2})$] and the ratio of P_w to P_s:

$$H = \Delta\left(\delta^{13}C_{CO2}\right) - 0.82\left[\ln\left(P_w / P_s\right)\right] + 0.73 \quad (1)$$

In Equation 1, the variable $\Delta(\delta^{13}C_{CO2})$ is a function of latitude (L) in the northern hemisphere and can be described by the following relationship (Keeling et al., 2001):

$$\Delta\left(\delta^{13}C_{CO2}\right) = 0.01L + 0.13 \quad (2)$$

To adapt this model (Equation 1) to the Nanning Basin $\delta^{13}C$ records, we substituted Equation 2 in Equation 1 and rearranged the equation to produce a summer to winter seasonal precipitation ratio (P_s/P_w):

$$P_s / P_w = 1 / e^{\wedge}\left[\left(H + 0.01L - 0.6\right) / -0.82\right] \quad (3)$$

Because total annual precipitation is the sum of P_s and P_w:

$$P_{total} = P_s + P_w \quad (4)$$

we can insert Equation 4 into Equation 3 and solve for P_w to produce an estimate of seasonal precipitation given an estimate of P_{total}:

$$P_w = \left(R\right) * \left(P_{total}\right) / \left(1 + R\right) \quad (5)$$

where

$$R = e^{\wedge}\left[\left(H + 0.01L - 0.6\right) / -0.82\right] \quad (6)$$

Substitution of a calculated value of P_w (Equations 5–6) into Equation 4 allows for calculation of P_s. A more detailed derivation of these equations is provided in the supporting information. In this study, we report proxy results for the P_s/P_w ratio (Equation 3) and for estimates of P_w and P_s (Equations 4–6).

2.4. Monte Carlo Error Propagation

We used a Monte Carlo resampling approach to propagate uncertainties through the proxy system model equations (Equations 1–6), which allows us to calculate a 95% confidence interval (C.I.) for estimates of the P_s/P_w ratio and estimates of P_s and P_w amounts. This method is analogous to best practices in atmospheric CO_2 proxy application (e.g., Breecker, 2013; Cui & Schubert, 2016; Franks et al., 2014; Royer et al., 2014; Steinthorsdottir et al., 2021). The Monte Carlo approach involves resampling each independent variable a large number of times (here, 10,000). These 10,000 resamples are then entered into the proxy equation, thereby generating 10,000 solutions. We take the median of these solutions to represent the proxy estimate,

and as reported elsewhere, this value tends to be similar to the result when the equations are solved without Monte Carlo resampling (Steinthorsdottir et al., 2021). A 95% C.I. is reported as the 2.5th and 97.5th quantiles of the 10,000 proxy solutions and offers a robust estimate of uncertainty.

The calculation of P_s/P_w ratios (Equation 3) involves two independent variables: intra-ring $\delta^{13}C$ amplitude (H) and latitude. To calculate a P_s/P_w ratio for each growth ring, we used a normally distributed sample of H values centered on the measured H value for the ring in question with a standard deviation defined as ±10% of the H value. We chose this conservative estimate of uncertainty because Schubert and Jahren (2011) found that an average of ~10 $\delta^{13}C$ measurements per growth ring obtains ~80% of the true H value. Our high resolution sampling resulted in an average of 14 and 25 samples for the modern and fossil growth rings, respectively, suggesting that we have likely captured an accurate H signal for each ring. When calculating P_s/P_w ratios for each growth ring, we defined latitude as a normally distributed sample centered on the modern latitude (22.8°N) with a standard deviation of 0.1° given that the location of the living trees is well constrained. For late Oligocene paleolatitude, we defined a normal distribution centered on the modern latitude of Nanning but with a wider distribution (±5° standard deviation). This paleolatitude was chosen because the South China Block has remained at or near its current latitude since the early Cenozoic (Wu et al., 2017).

A consensus P_s/P_w ratio was separately calculated for 1) the two modern tree cores, and 2) for the collection of fossil samples. Here, the H values are taken as the set of measured H values across the modern tree cores ($n = 22$) and the three fossil specimens ($n = 19$). Due to the relatively low number of samples in each of these groups, we opted to perform a bootstrap resampling (sampling with replacement) in order to preserve the characteristics of the H distributions without assuming normality. The consensus P_s/P_w estimate for each of the modern tree cores was calculated as the median and 95% C.I. of the 10,000 solutions for each core (QSX21A and QSX24A). The consensus P_s/P_w estimate for the fossil wood was taken as the median and 95% C.I. of the 10,000 solutions for the 19 fossil growth rings.

We calculated P_s and P_w amounts using an estimation of P_{total} values (Equations 4–6). For both the modern and fossil rings, we used the mean and standard deviation (1,296 ± 227 mm) of P_{total} values from the Nanning weather station (China Meteorological Data Service Center, Station No. 59431, years 1951–2016; Figure 1). We then ran a Monte Carlo resampling to solve Equation 3 using the same approach described for P_s/P_w ratios that were calculated on a per-ring basis, using the same normally distributed resamples of H and latitude for each ring. We used the long-term weather station P_{total} value rather than observed annual precipitation totals when calculating P_s and P_w estimates for each ring in the modern tree cores because annually resolved P_{total} values are unknown in the late Oligocene. Thus, holding the distribution of P_{total} values constant between modern and fossil wood allows us to directly compare proxy results and uncertainty on both modern and late Oligocene growth rings. We note that because P_{total} is independent of P_s/P_w (Equation 3), higher values of P_{total} serve to increase estimates of P_w and P_s, but proportionally, such that the ratio of P_s to P_w remains unchanged. Therefore, any independent estimates of late Oligocene P_{total} values that are better constrained in future studies may use the P_s/P_w ratios in this study to better refine P_s and P_w estimates for Nanning the late Oligocene.

Consensus P_s and P_w estimates were calculated for the modern and fossil trees using the same approach as P_s/P_w ratios: H values were bootstrapped and then 10,000 P_w solutions were calculated from the resamples. The resamples were combined for the modern trees, generating a set of 20,000 solutions from which a median and 95% C.I. for P_w were calculated. For the late Oligocene consensus P_w estimates, 10,000 solutions were generated from resampling of the 19 fossil growth rings. P_s values were calculated as the difference between P_{total} resamples and the P_w solutions.

A code and data file are available in the supporting information to allow for reproduction of our Monte Carlo analyses.

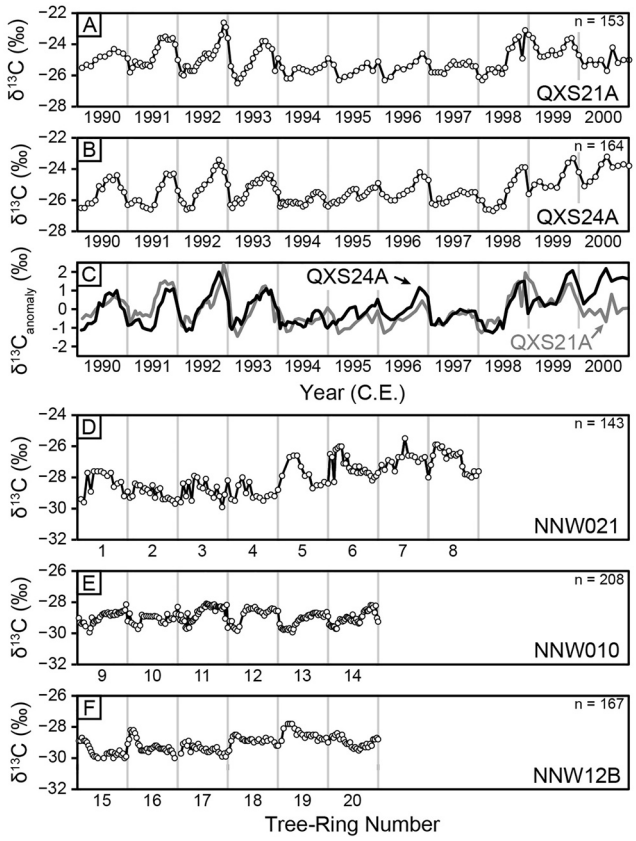

Figure 2. (a–c) Profiles of $\delta^{13}C$ values across modern and (d–f) fossil wood. (a and b) $\delta^{13}C$ profiles across modern *Pinus massioniana* tree cores. (c) $\delta^{13}C$ profiles normalized to the average of each sample. (d–f) $\delta^{13}C$ profiles across fossil evergreen wood; note that each profile represents a different fossil, and consequently rings are not correlated across the three fossil specimens. Gray vertical lines indicate ring boundaries. Number of analyses (n) is indicated in upper right of each panel; sample name is indicated in lower right of each panel.

3. Results

3.1. Development of High-Resolution $\delta^{13}C$ Profiles

The $\delta^{13}C$ values of the two modern *P. massoniana* tree cores differed significantly across the entire 1990–2000 series (Wilcoxon rank sum test, $p < 0.001$) (Figures 2a and 2b), which is common for neighboring modern trees, even of the same species (e.g., Leavitt & Long, 1984). However, normalized $\delta^{13}C$ records of the modern wood showed the relative changes in $\delta^{13}C$ value to be consistent across individuals (Figure 2c). On average, the late Oligocene wood fossils had significantly lower $\delta^{13}C$ values than the modern wood (Kruskall-Wallis rank sum test, $p < 0.001$) (Figures 2d–2f), consistent with preferential preservation of lignin relative to cellulose (Lukens et al., 2019a) and/or higher atmospheric CO_2 levels in the Oligocene relative to today (Foster et al., 2017; Schubert & Jahren, 2012). Notably, the fossil wood showed a similar quasi-periodic intra-ring $\delta^{13}C$ pattern to the modern wood, consistent with the evergreen habit inferred for the specimens based on previous work (Huang et al., 2018; Schubert & Jahren, 2011). Further, the amplitude of $\delta^{13}C$ values (H, Equation 5) across each ring was not statistically different between the modern and fossil tree-rings (Kruskall-Wallis rank sum test, $p = 0.27$).

The intra-ring patterns of $\delta^{13}C$ were compared between modern and fossil wood samples. Median and standard deviations of H for the three fossils were as follows: NNW021 = 2.0 ± 0.7‰, NNW010 = 1.5 ± 0.2‰, and NNW12B = 1.4 ± 0.5‰. Median and standard deviations of H for the cores from the two living tress are as follows: QXS21A = 1.5 ± 0.9‰ and QXS24A = 1.9 ± 0.7‰. The Kruskall-Wallis rank sum test run on these data resulted in no significant difference between mean ranks (chi-square = 5.1517, degrees of freedom = 4, $p = 0.27$). We note that the first growth ring analyzed in fossil sample NNW12B (labeled as ring 15 in Figure 2) was omitted from further analyses due to the peak $\delta^{13}C$ value occurring at the start of the ring.

3.2. P_s/P_w Ratios and Proxy Validation

Figure 3 compares the observed P_s/P_w ratios from the Nanning weather station record (1951–2016 CE) and the calculated P_s/P_w ratios for modern and fossil wood using the Monte Carlo approach. The P_s/P_w ratios on record at the Nanning weather station have a median of 3.4 (95% C.I. = 1.5–5.4). The consensus P_s/P_w values calculated for each modern tree core are as follows: QSX21A = 3.9 (95% C.I. = 1.3–38.3) and QSX24A = 6.6 (95% C.I. = 1.8–30.7). The consensus P_s/P_w values calculated for the fossil samples is 3.4 (95% C.I. = 1.5–8.3). All median values calculated using the P_s/P_w proxy fall within the 95% C.I. of the weather station record.

P_s/P_w ratios and 95% C.I. were also calculated for each growth ring in the modern and fossil samples (Table 1). Six of the 20 modern growth rings resulted in relatively high P_s/P_w ratios: for example, the rings corresponding to the years 1992 and 1998 in each of the modern trees resulted in P_s/P_w ratios above 30 and 16, respectively. Although summer and winter rainfall totals were near average values in these 2 years, the H values of the corresponding growth rings were higher than any of the other years in the modern profiles (Figures 2a and 2b). These high H values result in low P_w estimates, but P_s estimates are on par with the other years in the record. These anomalous H values suggest that the proxy system model may result in over-estimates of P_s/P_w ratios for some individual years; however, the consensus estimates for each group capture an accurate approximation of the modern climatological state at Nanning. The P_s/P_w ratios of the fossil growth rings closely matched the patterns observed in the modern data—most values have a central tendency similar to the weather station at Nanning, with a positive skew due to a small number of samples (rings 5–7; Table 1) that have relatively high H values and therefore high P_s/P_w ratios.

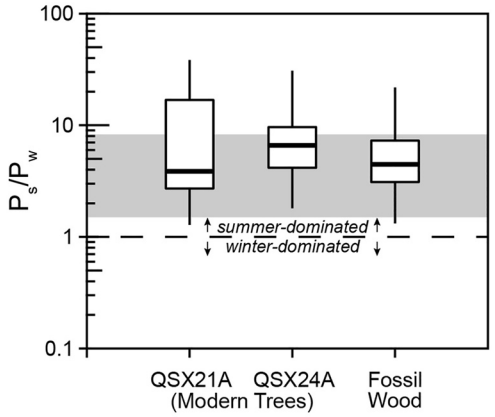

Figure 3. Validation of seasonal precipitation proxy. The ratio of summer precipitation (P_s: May through October) to winter precipitation (P_w: November through April) is plotted as a box and whisker plot, where the thick horizontal line is the median, the box shows the interquartile range, and the vertical whiskers span the 95% confidence interval (C.I.). The 95% C.I. for observed data from the Nanning weather station (1951–2016) is shown with gray shading. Calculated P_s/P_w ratios for two modern tree cores covering the period of 1990–2000 are shown individually to demonstrate variability between individual trees for overlapping time intervals. Fossil wood P_s/P_w values are calculated from a total of 19 growth rings without assuming temporal overlap between growth years.

3.3. Late Oligocene Precipitation Reconstruction

Using the modern climatological value and uncertainty for mean annual rainfall, the P_s/P_w ratios we report for southern China in the late Oligocene are consistent with median P_s = 1,042 mm (95% C.I.: 628–1,517 mm) and P_w = 235 (95% C.I.: 50–578 mm) (Figure 4; Table 1). The late Oligocene P_s and P_w values were indistinguishable from present-day seasonal precipitation measured at the local weather station, which has a median P_s of 977 mm (95% C.I.: 661–1,433 mm) and P_w of 292 mm (95% C.I.: 165–515 mm), and from application of this proxy on modern trees in Nanning, where P_s = 1,059 mm (95% C.I.: 617–1,558 mm) and P_w = 188 mm (95% C.I.: 31–583 mm). The consensus P_s and P_w estimates for the modern and fossil trees have 95% C.I. that do not overlap, providing a clear signal of summer-dominated rainfall both today and in the late Oligocene (Figure 4).

When calculating P_s and P_w for each fossil ring, we found that median P_s was greater than median P_w for all years, consistent with a summer-dominated precipitation regime for each of the years in which these trees grew during the late Oligocene (Table 1). These confidence intervals do not overlap for P_s and P_w values for nearly every individual growth ring from the late Oligocene. These results suggest that the strength and inter-annual variability of summer precipitation in the late Oligocene was similar to modern conditions.

Using these results, we calculate conservative summer rainfall rates during the late Oligocene of 5.7 mm/day (95% C.I. = 3.4–8.2), with P_s = 81% of P_{total} on average. This estimate closely matches present-day values at the site (median = 5.3, 95% C.I. = 3.6–7.8 mm/day; P_s = 77% of P_{total} for 1951–2016 CE). Because these daily rainfall rates represent 6-month averages, these values likely underestimate maximum daily rainfall rates during peak monsoon months. Nevertheless, these values exceed the threshold for monsoon climates defined by Wang and LinHo (2002) (≥3.0 mm/day and $P_s \geq$ 55% of P_{total}), and provide firm quantitative evidence for a paleo-monsoon using the metrics employed in modern climatology.

4. Discussion

4.1. Sensitivity and Refinement of the Proxy System Model

Our analyses represent the most rigorous testing of uncertainty in the Schubert and Jahren (2011) proxy system model to date. Regardless, the proxy should continue to be improved with future work. First, the current form of the seasonal precipitation proxy uses a constant of 0.73‰ to represent post-photosynthetic processes in evergreen trees (Equation 1; see supporting information), such as starch remobilization (Schubert & Jahren, 2011). Recent work suggests that this value may be variable rather than constant (e.g., Gessler et al., 2014; Guerrieri et al., 2019). Future work should constrain a range of possible values for this parameter or develop quantitative relationships that could be incorporated into the proxy system model to improve the global applicability and robustness of the proxy.

Second, the estimate of P_s/P_w ratios and seasonal precipitation totals relies on knowledge of the annual cycle of $\delta^{13}C_{CO2}$ ($\Delta(\delta^{13}C_{CO2})$, Equation 2). To address uncertainty in this component of the proxy, we performed a sensitivity analysis to test whether varying $\Delta(\delta^{13}C_{CO2})$ would impact our interpretations of rainfall seasonality given the measured H values. The slope and intercept of Equation 2 are fitted to the modern pattern of annual variations in $\delta^{13}C_{CO2}$ value for the northern hemisphere, where $\Delta(\delta^{13}C_{CO2})$ increases with northing latitude. This relationship is driven by seasonal exchanges of C between the biosphere and atmosphere: photosynthesis in the boreal summer depletes the atmosphere in ^{12}C and enriches the remaining CO_2 in ^{13}C, followed by a wintertime release of ^{12}C back to the atmosphere as a result of soil respiration and reduced productivity (Keeling et al., 2005). The paleogeography of the Oligocene (e.g., Kennedy-Asser et al., 2019) suggests that northern hemisphere net primary productivity may have been enhanced relative to today,

Table 1
(Paleo)climate Estimations for Modern and Late Oligocene Tree Rings From Nanning, China

							P_w		P_s		P_s/P_w	
Sample	Year	P_{total}	P_w (obs.)	P_s (obs.)	P_s/P_w (obs.)	H (‰)	(Pred.)	(95% CI)	(Pred.)	(95% CI)	(Pred.)	(95% CI)
Modern tree-rings, weather station data, and proxy results												
QXS21A	1990	1,095	423	672	1.6	1.2	347	(220, 500)	939	(611, 1,285)	3.1	(2.0, 3.6)
QXS21A	1991	1,198	201	996	5.0	2.3	115	(60, 207)	1,170	(763, 1,588)	13.3	(5.9, 17.3)
QXS21A	1992	1,238	307	931	3.0	3.4	33	(13, 76)	1,254	(817, 1695)	57.5	(16.8, 86.1)
QXS21A	1993	1,285	383	902	2.4	2.7	72	(35, 142)	1,213	(787, 1,643)	23.2	(8.9, 31.9)
QXS21A	1994	1,736	279	1,458	5.2	1.3	322	(197, 472)	964	(624, 1,315)	3.5	(2.2, 4.0)
QXS21A	1995	1,272	306	966	3.2	1.2	330	(204, 484)	956	(622, 1,307)	3.4	(2.1, 3.9)
QXS21A	1996	1,191	255	936	3.7	1.7	205	(118, 328)	1,079	(707, 1,468)	6.5	(3.5, 8.0)
QXS21A	1997	1,453	533	920	1.7	0.8	465	(299, 648)	822	(533, 1,121)	2.0	(1.4, 2.2)
QXS21A	1998	1,286	278	1,007	3.6	3.2	39	(16, 86)	1,248	(812, 1,689)	47.2	(14.9, 69.7)
QXS21A	1999	1,113	186	927	5.0	0.6	563	(366, 768)	727	(472, 988)	1.4	(1.1, 1.5)
QXS21A	2000	1,051	312	739	2.4	1.5	263	(158, 398)	1,021	(663, 1,397)	4.6	(2.7, 5.5)
QXS24A	1990	1,095	423	672	1.6	2.1	135	(73, 235)	1,147	(749, 1,559)	10.9	(5.1, 13.9)
QXS24A	1991	1,198	201	996	5.0	2.2	120	(63, 216)	1,166	(757, 1,582)	12.6	(5.7, 16.5)
QXS24A	1992	1,238	307	931	3.0	3.2	40	(17, 90)	1,245	(814, 1,686)	45.1	(14.3, 66)
QXS24A	1993	1,285	383	902	2.4	2.2	126	(68, 226)	1,158	(752, 1,571)	11.8	(5.3, 15.4)
QXS24A	1994	1,736	279	1,458	5.2	1.0	422	(271, 593)	865	(562, 1,181)	2.3	(1.6, 2.6)
QXS24A	1995	1,272	306	966	3.2	1.5	248	(148, 378)	1,036	(677, 1,415)	5.0	(2.9, 6.0)
QXS24A	1996	1,191	255	936	3.7	1.7	207	(121, 332)	1,077	(697, 1,467)	6.4	(3.4, 7.8)
QXS24A	1997	1,453	533	920	1.7	0.9	458	(294, 638)	830	(542, 1,132)	2.0	(1.5, 2.2)
QXS24A	1998	1,286	278	1,007	3.6	2.7	71	(34, 140)	1,215	(793, 1,648)	23.6	(8.8, 32.1)
QXS24A	1999	1,113	186	927	5.0	1.9	168	(94, 277)	1,117	(727, 1,517)	8.4	(4.2, 10.5)
QXS24A	2000	1,051	312	739	2.4	1.9	171	(97, 286)	1,113	(723, 1,516)	8.1	(4.1, 10.2)
Late Oligocene fossil wood and paleoclimate proxy results												
NNW021	Ring1	1,296	–	–		1.3	312	(193, 461)	974	(634, 1326)	3.7	(2.2, 4.3)
NNW021	Ring2	1,296	–	–		0.9	443	(286, 619)	845	(549, 1,154)	2.2	(1.5, 2.4)
NNW021	Ring3	1,296	–	–		1.7	212	(122, 331)	1,074	(699, 1,464)	6.3	(3.3, 7.7)
NNW021	Ring4	1,296	–	–		2.0	154	(86, 261)	1,130	(736, 1,538)	9.4	(4.4, 12.0)
NNW021	Ring5	1,296	–	–		2.9	56	(25, 117)	1,230	(799, 1,668)	31.2	(10.6, 44.5)
NNW021	Ring6	1,296	–	–		2.8	63	(29, 126)	1,223	(796, 1,654)	27.4	(9.8, 38.2)
NNW021	Ring7	1,296	–	–		2.7	71	(34, 138)	1,214	(794, 1,649)	23.9	(8.8, 32.7)
NNW021	Ring8	1,296	–	–		2.1	137	(76, 237)	1,146	(749, 1,556)	10.7	(4.9, 13.8)
NNW010	Ring9	1,296	–	–		1.9	172	(98, 283)	1,112	(723, 1,513)	8.1	(4, 10.3)
NNW010	Ring10	1,296	–	–		1.4	284	(174, 427)	1,000	(652, 1,365)	4.2	(2.5, 5.0)
NNW010	Ring11	1,296	–	–		1.6	234	(140, 362)	1,049	(686, 1,431)	5.5	(3.0, 6.7)
NNW010	Ring12	1,296	–	–		1.6	235	(139, 364)	1,051	(684, 1,434)	5.5	(3.0, 6.7)
NNW010	Ring13	1,296	–	–		1.3	313	(193, 460)	973	(636, 1,326)	3.7	(2.2, 4.3)
NNW010	Ring14	1,296	–	–		1.5	257	(156, 393)	1,026	(669, 1,404)	4.8	(2.7, 5.8)
NNW12B	Ring16	1,296	–	–		1.9	172	(97, 281)	1,113	(724, 1,521)	8.1	(4.0, 10.3)
NNW12B	Ring17	1,296	–	–		1.3	313	(192, 462)	973	(634, 1,322)	3.7	(2.2, 4.3)
NNW12B	Ring18	1,296	–	–		1.4	285	(175, 426)	1,000	(653, 1,367)	4.2	(2.5, 5.0)

Table 1
Continued

Sample	Year	P_{total}	P_w (obs.)	P_s (obs.)	P_s/P_w (obs.)	H (‰)	P_w (Pred.)	P_w (95% CI)	P_s (Pred.)	P_s (95% CI)	P_s/P_w (Pred.)	P_s/P_w (95% CI)
NNW12B	Ring19	1,296	–	–		1.4	285	(174, 426)	1,001	(651, 1,361)	4.2	(2.4, 5.0)
NNW12B	Ring20	1,296	–	–		0.6	555	(359, 758)	733	(478, 1,000)	1.5	(1.1, 1.6)

Note. Predicted values for P_w and P_s are shown as the median of Monte Carlo resampling, with 95% confidence intervals (CI). Ring 15 (the first ring in NNW12B) was omitted from analysis; see text for details. Abbreviations are as follows. P_{total}, total precipitation; P_w, winter precipitation (November–April); P_s, summer precipitation (May–October), obs., observed data from weather station; pred., proxy-derived prediction.

given 1) the lack of a permanent arctic ice cap, meaning more vegetation cover in the northern hemisphere and longer growing seasons, and 2) continent positions were largely similar to modern conditions, with a majority of land positioned in the northern hemisphere. We tested the sensitivity of $\Delta(\delta^{13}C_{CO2})$ on seasonal precipitation estimates by varying this term in Equation 1 from 0.0‰ (no annual change in $\delta^{13}C_{CO2}$) to 2.0‰ (twice the maximum possible value of $\delta^{13}C_{CO2}$ under modern conditions). We found that for all measured H values, the ratio of estimated summer precipitation is little affected by an enhanced annual $\Delta(\delta^{13}C_{CO2})$ cycle (Figure 5), and mean H values would still be consistent with summer-dominated precipitation even under greatly reduced $\Delta(\delta^{13}C_{CO2})$. We therefore conclude that the signal of summer-dominated precipitation in the late Oligocene is robust.

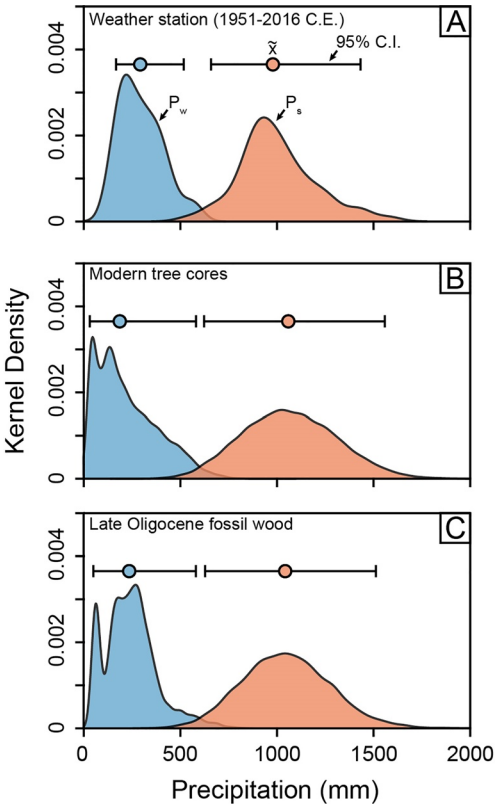

Figure 4. Kernel density functions plotted for winter (P_w, blue) and summer precipitation (P_s, red). Colored circles indicate the median ($\tilde{x}$) and 95% confidence intervals (C.I., horizontal lines) for P_w and P_s. (a) Instrument record for Nanning weather station. Data are plotted for 1951–2016 CE. (b) Consensus seasonal precipitation estimates from all 22 of the modern growth rings (11 rings per tree core). (c) Consensus seasonal precipitation estimates from 19 fossil growth rings. Note that in all panels, $P_s > P_w$ for each year, median P_s and P_w values overlap across each group (a–c), and the 95% C.I. do not overlap for any group.

4.2. Implications for EAM Evolution

Most studies that investigate monsoon systems in the geologic record focus on Quaternary records or rely on climate models to assess monsoon intensity and variability (Wang et al., 2017). Estimates of monsoon characteristics in deep-time using traditional mean annual precipitation proxies such as stable isotopes in paleosols and fossil teeth (Passey, 2012), leaf morphometrics (Peppe et al., 2011), floral assemblages (Utescher et al., 2014), paleosol magnetics (Maxbauer et al., 2016), and paleosol bulk geochemistry (Lukens et al., 2019b; Stinchcomb et al., 2016), might be biased within monsoon regions that receive a large proportion of their annual precipitation within a few weeks or months, or during time intervals wherein spatial variability of isotopes in meteoric water may fundamentally alter isotope-precipitation relationships (e.g., Johnson & Ingram, 2004). These proxies can provide important information on long-term climate trends for a particular region (i.e., the EAM; Wang et al., 2019); however, resolving inter- or intra-annual precipitation patterns that are characteristic of monsoon systems is much more challenging.

Our analyses of modern and fossil wood $\delta^{13}C$ profiles show similar overall patterns that are characteristic of evergreen trees growing in a strongly seasonal climate (Schubert & Jahren, 2011). This interpretation is supported by paleobotanical analyses from the Santang fossil assemblage by Huang et al. (2018). The wood fossils of the Fagaceae family have predominantly faint to absent growth rings, though some samples have distinct ring boundaries (such as those in this study; Figures 1f–1h). Importantly, though, some of the *Castanopsis* specimens in the fossil assemblage show indistinct growth ring boundaries with ring-porous patterns, which are features that have been observed in *Castanopsis* living today in Meghalaya, India (Sharma et al., 2011) and northern Thailand (Phromprasit et al., 2016). Both of these areas have strongly seasonal precipitation un-

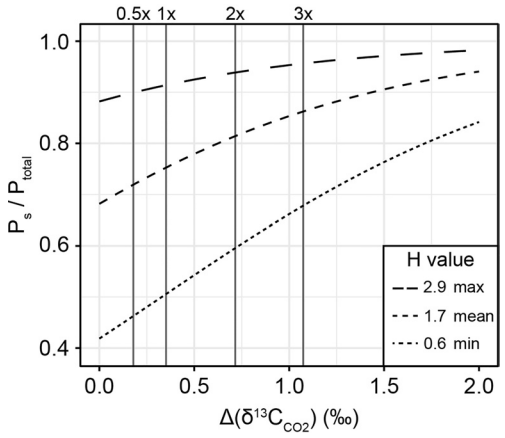

Figure 5. The fraction of summer precipitation to total annual precipitation (P_s/P_{total}) as a function of annual variation in atmospheric $\delta^{13}C_{CO2}$ value ($\Delta(\delta^{13}C_{CO2})$). The maximum, minimum, and mean H values for Nanning wood fossils are shown. At the modern latitude of Nanning, China (22.8°N), the $\Delta(\delta^{13}C_{CO2})$ value is 0.35‰ (vertical line at 1X). Note that a doubling (2X) or tripling (3X) of this magnitude of $\delta^{13}C_{CO2}$ variation has relatively little effect and only increases estimates of summer rainfall proportions. Reduction of $\Delta(\delta^{13}C_{CO2})$ also has little effect the interpretation of late Oligocene summer-dominated rainfall. Note that P_s/P_{total} values >0.5 indicate summer-dominated rainfall.

der the South Asian Monsoon. However, the *Castanopsis* fossils with distinct ring boundaries that lack ring porosity are possibly similar to those living in subtropical, EAM-affected areas of modern Japan, Taiwan, and continental China (Huang et al., 2018). Collectively, the Santang wood fossils are consistent with our interpretation of monsoon-style precipitation patterns in southern China during the late Oligocene. The use of modern P_{total} values for estimating late Oligocene seasonal precipitation amounts is supported by pollen and plant macrofossils associated with the Nanning fossil wood deposit that were similar to extant flora in the area and were consistent with warm-temperate and humid conditions (Ying et al., 2018). Further, the presence of sub-humid to humid climates interpreted for the now-arid interior of China during the late Oligocene indicates that southeast China was at least as wet (P_{total} > 1,000 mm) (Miao et al., 2013).

Our results suggest that strong seasonality of rainfall in southern China may have been a feature of a late Oligocene EAM system. This interpretation broadly agrees with the prevailing model of a weak EAM beginning in the Eocene (Licht et al., 2014; Quan et al., 2012; Xie et al., 2019, 2020) and gradually transitioning to a monsoon system at least as strong as today during the Miocene (Ding et al., 2021; Sun & Wang, 2005; Tada et al., 2016). The paleoclimate estimates we report help to fill a substantial data gap from the late Oligocene in southern and eastern China compared to the Eocene and Miocene (Guo et al., 2008; Sun & Wang, 2005; Tada et al., 2016). Indeed, the lack of quantitative paleoclimate estimates from the late Oligocene has resulted in studies generalizing the initiation of the EAM to be near the Paleogene-Neogene boundary, but without the ability to provide more precise estimates of EAM behavior in the Oligocene (e.g., Farnsworth et al., 2019; Li et al., 2021; Sun & Wang, 2005).

A defining feature of the EAM is a seasonal reversal from warm, moist southeasterlies in the summer to cool, dry northwesterlies in the winter (Wang & LinHo, 2002). This pattern requires a disruption of the westerlies by the Tibetan Plateau, which began around the late Oligocene as terranes in the central to northern portions of the orographic province attained elevations above 3–3.5 km (Fang et al., 2020; Li et al., 2021; Wang et al., 2020). Modeling experiments by Li et al. (2021) revealed that when central Tibet reaches >3 km, a transition occurs wherein deciduous broadleaf vegetation of southeastern Asia are replaced by evergreen broadleaf communities. The Oligocene paleofloras of Nanning nearby Ningming (also Oligocene in age) are the oldest such evergreen broadleaf assemblages in the region, both of which show clear paleobotanical affinities for warm, wet, and seasonal conditions (Dong et al., 2018; Huang et al., 2018; Shi et al., 2012; Shi et al., 2014; Ying et al., 2018).

5. Conclusions

The Oligocene remains a markedly understudied interval in monsoon paleoclimatology of southern and eastern Asia. The high-resolution $\delta^{13}C$ records from late Oligocene wood fossils presented in this study help to fill a critical gap in paleoprecipitation data from southern China. We report a robust record of summer-dominated rainfall for each of the 19 fossil rings we analyzed, consistent with 11 years of high resolution $\delta^{13}C$ profiles from two living trees growing nearby. We suggest that these patterns indicate the presence of an EAM-style system in the late Oligocene that had similar strength and seasonality to modern conditions, but further work is needed to connect these rainfall reconstructions with mechanisms of monsoon system evolution.

Data Availability Statement

Data sets for this research are available in the supporting information and also at https://doi.pangaea.de/10.1594/PANGAEA.919141.

Acknowledgments
We thank Dr. Yingfeng Xu for laboratory assistance and Dr. Keyan Fang for providing modern *Pinus massoniana* wood samples. This research was supported by U.S. National Science Foundation (grant no. AGS-1903601) and subaward grant #330175-01 from the University of Louisiana at Lafayette. Fieldwork was supported by Natural Science Foundation of China (nos. 41820104002 and 41888101).

References

Aggarwal, P. K., Fröhlich, K., Kulkarni, K. M., & Gourcy, L. L. (2004). Stable isotope evidence for moisture sources in the Asian summer monsoon under present and past climate regimes. *Geophysical Research Letters*, *31*, L08203. https://doi.org/10.1029/2004GL019911

Beck, J. W., Zhou, W., Li, C., Wu, Z., White, L., Xian, F., et al. (2018). A 550,000-year record of East Asian monsoon rainfall from ^{10}Be in loess. *Science*, *360*, 877. https://doi.org/10.1126/science.aam5825

Bougeois, L., de Rafélis, M., Reichart, G.-J., De Nooijer, L. J., Nicollin, F., & Dupont-Nivet, G. (2014). A high resolution study of trace elements and stable isotopes in oyster shells to estimate Central Asian Middle Eocene seasonality. *Chemical Geology*, *363*, 200–212. https://doi.org/10.1016/j.chemgeo.2013.10.037

Bougeois, L., Dupont-Nivet, G., de Rafélis, M., Tindall, J. C., Proust, J.-N., Reichart, G.-J., et al. (2018). Asian monsoons and aridification response to Paleogene sea retreat and Neogene westerly shielding indicated by seasonality in Paratethys oysters. *Earth and Planetary Science Letters*, *485*, 99–110. https://doi.org/10.1016/j.epsl.2017.12.036

Breecker, D. O. (2013). Quantifying and understanding the uncertainty of atmospheric CO_2 concentrations determined from calcic paleosols. *Geochemistry, Geophysics, Geosystems*, *14*(8), 3210–3220. https://doi.org/10.1002/ggge.20189

Cheng, H., Edwards, R. L., Sinha, A., Spötl, C., Yi, L., Chen, S., et al. (2016). The Asian monsoon over the past 640,000 years and ice age terminations. *Nature*, *534*, 640–646. https://doi.org/10.1038/nature18591

Clift, P. D., Hodges, K. V., Heslop, D., Hannigan, R., Van Long, H., & Calves, G. (2008). Correlation of Himalayan exhumation rates and Asian monsoon intensity. *Nature Geoscience*, *1*, 875. https://doi.org/10.1038/ngeo351

Cui, Y., & Schubert, B. A. (2016). Quantifying uncertainty of past pCO_2 determined from changes in C_3 plant carbon isotope fractionation. *Geochimica et Cosmochimica Acta*, *172*, 127–138. https://doi.org/10.1016/j.gca.2015.09.032

Cui, Y., Schubert, B. A., & Jahren, A. H. (2020). A 23 m.y. record of low atmospheric CO_2. *Geology*, *48*, 888–892.

Ding, W., Hou, D., Gan, J., Wu, P., Zhang, M., & George, S. C. (2021). Palaeovegetation variation in response to the late Oligocene-early Miocene East Asian summer monsoon in the Ying-Qiong Basin, South China Sea. *Palaeogeography, Palaeoclimatology, Palaeoecology*, *567*, 110205. https://doi.org/10.1016/j.palaeo.2020.110205

Dong, J.-L., Sun, B.-N., Mao, T., Liu, C.-H., Wang, X.-L., Sun, M.-X., et al. (2018). The occurrence of Burretiodendron from the Oligocene of South China and its geographic analysis. *Palaeogeography, Palaeoclimatology, Palaeoecology*, *512*, 95–105. https://doi.org/10.1016/j.palaeo.2017.07.004

Evans, M. N., Tolwinski-Ward, S. E., Thompson, D. M., & Anchukaitis, K. J. (2013). Applications of proxy system modeling in high resolution paleoclimatology. *Quaternary Science Reviews*, *76*, 16–28. https://doi.org/10.1016/j.quascirev.2013.05.024

Fang, X., Dupont-Nivet, G., Wang, C., Song, C., Meng, Q., Zhang, W., et al. (2020). Revised chronology of central Tibet uplift (Lunpola Basin). *Science Advances*, *6*, eaba7298. https://doi.org/10.1126/sciadv.aba7298

Farnsworth, A., Lunt, D. J., Robinson, S. A., Valdes, P. J., Roberts, W. H. G., Clift, P. D., et al. (2019). Past East Asian monsoon evolution controlled by paleogeography, not CO_2. *Science Advances*, *5*, eaax1697. https://doi.org/10.1126/sciadv.aax1697

Fleitmann, D., Burns, S. J., Mudelsee, M., Neff, U., Kramers, J., Mangini, A., & Matter, A. (2003). Holocene Forcing of the Indian Monsoon recorded in a stalagmite from Southern Oman. *Science*, *300*, 1737–1739. https://doi.org/10.1126/science.1083130

Foster, G. L., Royer, D. L., & Lunt, D. J. (2017). Future climate forcing potentially without precedent in the last 420 million years. *Nature Communications*, *8*, 14845. https://doi.org/10.1038/ncomms14845

Franks, P. J., Royer, D. L., Beerling, D. J., Van de Water, P. K., Cantrill, D. J., Barbour, M. M., & Berry, J. A. (2014). New constraints on atmospheric CO_2 concentration for the Phanerozoic. *Geophysical Research Letters*, *41*(13), 4685–4694. https://doi.org/10.1002/2014gl060457

Gessler, A., Ferrio, J. P., Hommel, R., Treydte, K., Werner, R. A., & Monson, R. K. (2014). Stable isotopes in tree rings: Towards a mechanistic understanding of isotope fractionation and mixing processes from the leaves to the wood. *Tree Physiology*, *34*(8), 796–818. https://doi.org/10.1093/treephys/tpu040

Guerrieri, R., Belmecheri, S., Ollinger, S. V., Asbjornsen, H., Jennings, K., Xiao, J., et al. (2019). Disentangling the role of photosynthesis and stomatal conductance on rising forest water-use efficiency. *Proceedings of the National Academy of Sciences of the United States of America*, *116*(34), 16909–16914. https://doi.org/10.1073/pnas.1905912116

Guo, Z. T., Sun, B., Zhang, Z. S., Peng, S. Z., Xiao, G. Q., Ge, J. Y., et al. (2008). A major reorganization of Asian climate by the early Miocene. *Climate of the Past*, *4*(3), 153–174. https://doi.org/10.5194/cp-4-153-2008

Huang, L., Jin, J., Quan, C., & Oskolski, A. A. (2018). Mummified fossil woods of Fagaceae from the upper Oligocene of Guangxi, South China. *Journal of Asian Earth Sciences*, *152*, 39–51. https://doi.org/10.1016/j.jseaes.2017.11.029

Johnson, K. R., & Ingram, B. L. (2004). Spatial and temporal variability in the stable isotope systematics of modern precipitation in China: Implications for paleoclimate reconstructions. *Earth and Planetary Science Letters*, *220*, 365–377. https://doi.org/10.1016/S0012-821X(04)00036-6

Judd, E. J., Ivany, L. C., DeConto, R. M., Halberstadt, A. R. W., Miklus, N. M., Junium, C. K., & Uveges, B. T. (2019). Seasonally resolved proxy data from the Antarctic Peninsula support a heterogeneous middle Eocene Southern Ocean. *Paleoceanography and Paleoclimatology*, *34*, 787–799. https://doi.org/10.1029/2019PA003581

Kathayat, G., Cheng, H., Sinha, A., Yi, L., Li, X., Zhang, H., et al. (2017). The Indian monsoon variability and civilization changes in the Indian subcontinent. *Science Advances*, *3*, e1701296. https://doi.org/10.1126/sciadv.1701296

Keeling, C. D., Piper, S. C., Bacastow, R. B., Wahlen, M., Whorf, T. P., Heimann, M., & Meijer, H. A. (2001). *Exchanges of atmospheric CO_2 and $^{13}CO_2$ with the terrestrial biosphere and oceans from 1978 to 2000. I. Global aspects.* San Diego, CA: Scripps Institution of Oceanography.

Keeling, C. D., Piper, S. C., Bacastow, R. B., Wahlen, M., Whorf, T. P., Heimann, M., & Meijer, H. A. (2005). Atmospheric CO_2 and $^{13}CO_2$ exchange with the terrestrial biosphere and oceans from 1978 to 2000: Observations and carbon cycle implications. In J. R. Ehleringer, T. Cerling, & D. M. Denise (Eds.), *A history of atmospheric CO_2 and its effects on plants, animals, and ecosystems* (pp. 83–113). Springer.

Kennedy-Asser, A. T., Lunt, D. J., Farnsworth, A., & Valdes, P. J. (2019). Assessing mechanisms and uncertainty in modeled climatic change at the Eocene-Oligocene transition. *Paleoceanography and Paleoclimatology*, *34*, 16–34. https://doi.org/10.1029/2018pa003380

Leavitt, S. W., & Long, A. (1984). Sampling strategy for stable carbon isotope analysis of tree rings in pine. *Nature*, *311*, 145–147. https://doi.org/10.1038/311145a0

Licht, A., van Cappelle, M., Abels, H. A., Ladant, J.-B., Trabucho-Alexandre, J., France-Lanord, C., et al. (2014). Asian monsoons in a late Eocene greenhouse world. *Nature*, *513*, 501–506. https://doi.org/10.1038/nature13704

Li, S.-F., Valdes, P. J., Farnsworth, A., Davies-Barnard, T., Su, T., Lunt, D. J., et al. (2021). Orographic evolution of northern Tibet shaped vegetation and plant diversity in eastern Asia. *Science Advances*, *7*(5), eabc7741.

Liu, Q., Deng, C., Torrent, J., & Zhu, R. (2007). Review of recent developments in mineral magnetism of the Chinese loess. *Quaternary Science Reviews*, *26*, 368–385. https://doi.org/10.1016/j.quascirev.2006.08.004
Liu, X., Dong, B., Yin, Z.-Y., Smith, R. S., & Guo, Q. (2017). Continental drift and plateau uplift control origination and evolution of Asian and Australian monsoons. *Scientific Reports*, *7*, 40344. https://doi.org/10.1038/srep40344
Li, X., Zhang, R., Zhang, Z., & Yan, Q. (2018). Do climate simulations support the existence of East Asian monsoon climate in the Late Eocene? *Palaeogeography, Palaeoclimatology, Palaeoecology*, *509*, 47–57. https://doi.org/10.1016/j.palaeo.2017.12.037
Loope, D. B., Rowe, C. M., & Joeckel, R. M. (2001). Annual monsoon rains recorded by Jurassic dunes. *Nature*, *412*, 64–66. https://doi.org/10.1038/35083554
Lukens, W. E., Eze, P., & Schubert, B. A. (2019a). The effect of diagenesis on carbon isotope values of fossil wood. *Geology*, *47*, 987–991. https://doi.org/10.1130/G46412.1
Lukens, W. E., Stinchcomb, G. E., Nordt, L. C., Kahle, D. J., Driese, S. G., & Tubbs, J. D. (2019b). Recursive partitioning improves paleosol proxies for rainfall. *American Journal of Science*, *319*, 819–845. https://doi.org/10.2475/10.2019.01
Maxbauer, D. P., Feinberg, J. M., & Fox, D. L. (2016). Magnetic mineral assemblages in soils and paleosols as the basis for paleoprecipitation proxies: A review of magnetic methods and challenges. *Earth-Science Reviews*, *155*, 28–48. https://doi.org/10.1016/j.earscirev.2016.01.014
Miao, Y. F., Fang, X. M., Wu, F. L., Cai, M. T., Song, C. H., Meng, Q. Q., & Xu, L. (2013). Late Cenozoic continuous aridification in the western Qaidam Basin: Evidence from sporopollen records. *Climate of the Past*, *9*(4), 1863–1877. https://doi.org/10.5194/cp-9-1863-2013
Passey, B. H. (2012). Reconstructing terrestrial environments using stable isotopes in fossil teeth and paleosol carbonates. *Paleontological Society Papers*, *18*, 167–194. https://doi.org/10.1017/S1089332600002606
Passey, B. H., Ayliffe, L. K., Kaakinen, A., Zhang, Z., Eronen, J. T., Zhu, Y., et al. (2009). Strengthened East Asian summer monsoons during a period of high-latitude warmth? Isotopic evidence from Mio-Pliocene fossil mammals and soil carbonates from northern China. *Earth and Planetary Science Letters*, *277*, 443–452. https://doi.org/10.1016/j.epsl.2008.11.008
Passey, B. H., Robinson, T. F., Ayliffe, L. K., Cerling, T. E., Sponheimer, M., Dearing, M. D., et al. (2005). Carbon isotope fractionation between diet, breath CO_2, and bioapatite in different mammals. *Journal of Archaeological Science*, *32*(10), 1459–1470. https://doi.org/10.1016/j.jas.2005.03.015
Peppe, D. J., Royer, D. L., Cariglino, B., Oliver, S. Y., Newman, S., Leight, E., et al. (2011). Sensitivity of leaf size and shape to climate: Global patterns and paleoclimatic applications. *The New Phytologist*, *190*, 724–739. https://doi.org/10.1111/j.1469-8137.2010.03615.x
Phromprasit, P., Vajrodaya, S., Vajrodaya, S., & Kermanee, P. (2016). Species identification of some Castanopsis (D.Don) Spach (Fagaceae) species from Northern Thailand using wood characteristics. *Thai Forest Bulletin, Botany*, *44*, 88–100. https://doi.org/10.20531/tfb.2016.44.2.01
Quade, J., Cerling, T. E., & Bowman, J. R. (1989). Development of Asian monsoon revealed by marked ecological shift during the latest Miocene in northern Pakistan. *Nature*, *342*, 163–166. https://doi.org/10.1038/342163a0
Quan, C., Fu, Q., Shi, G., Liu, Y., Li, L., Liu, X., & Jin, J. (2016). First Oligocene mummified plant Lagerstätte at the low latitudes of East Asia. *Science China Earth Sciences*, *59*, 445–448. https://doi.org/10.1007/s11430-015-5250-z
Quan, C., Liu, Y.-S., & Utescher, T. (2012). Eocene monsoon prevalence over China: A paleobotanical perspective. *Palaeogeography, Palaeoclimatology, Palaeoecology*, *365–366*, 302–311. https://doi.org/10.1016/j.palaeo.2012.09.035
R Core Team. (2020). *R: A language and environment for statistical computing*. Vienna, Austria: R Foundation for Statistical Computing.
Royer, D. L., Donnadieu, Y., Park, J., Kowalczyk, J., & Godderis, Y. (2014). Error analysis of CO_2 and O_2 estimates from the long-term geochemical model GEOCARBSULF. *American Journal of Science*, *314*(9), 1259–1283. https://doi.org/10.2475/09.2014.01
Schubert, B. A., & Jahren, A. H. (2011). Quantifying seasonal precipitation using high-resolution carbon isotope analyses in evergreen wood. *Geochimica et Cosmochimica Acta*, *75*, 7291–7303. https://doi.org/10.1016/j.gca.2011.08.002
Schubert, B. A., & Jahren, A. H. (2012). The effect of atmospheric CO_2 concentration on carbon isotope fractionation in C_3 land plants. *Geochimica et Cosmochimica Acta*, *96*, 29–43. https://doi.org/10.1016/j.gca.2012.08.003
Schubert, B. A., Jahren, A. H., Davydov, S. P., & Warny, S. (2017). The transitional climate of the late Miocene Arctic: Winter-dominated precipitation with high seasonal variability. *Geology*, *45*, 447–450. https://doi.org/10.1130/G38746.1
Schubert, B. A., Jahren, A. H., Eberle, J. J., Sternberg, L. S. L., & Eberth, D. A. (2012). A summertime rainy season in the Arctic forests of the Eocene. *Geology*, *40*, 523–526. https://doi.org/10.1130/G32856.1
Schubert, B. A., & Timmermann, A. (2015). Reconstruction of seasonal precipitation in Hawai'i using high-resolution carbon isotope measurements across tree rings. *Chemical Geology*, *417*, 273–278. https://doi.org/10.1016/j.chemgeo.2015.10.013
Sharma, C. L., Sharma, M., Carter, M. J., & Kharkongor, B. M. (2011). Inter species wood variation of *Castanopsis* species of Meghalaya. *Journal of the Indian Academy of Wood Science*, *8*, 124–129. https://doi.org/10.1007/s13196-012-0031-1
Shi, G.-L., Xie, Z.-M., & Li, H.-M. (2014). High diversity of Lauraceae from the Oligocene of Ningming, South China. *Palaeoworld*, *23*(3–4), 336–356. https://doi.org/10.1016/j.palwor.2014.08.001
Shi, G., Zhou, Z., & Xie, Z. (2012). A new Oligocene Calocedrus from South China and its implications for transpacific floristic exchanges. *American Journal of Botany*, *99*(1), 108–120. https://doi.org/10.3732/ajb.1100331
Spicer, R. A., Yang, J., Herman, A. B., Kodrul, T., Maslova, N., Spicer, T. E. V., et al. (2016). Asian Eocene monsoons as revealed by leaf architectural signatures. *Earth and Planetary Science Letters*, *449*, 61–68. https://doi.org/10.1016/j.epsl.2016.05.036
Spicer, R., Yang, J., Herman, A., Kodrul, T., Aleksandrova, G., Maslova, N., et al. (2017). Paleogene monsoons across India and South China: Drivers of biotic change. *Gondwana Research*, *49*, 350–363. https://doi.org/10.1016/j.gr.2017.06.006
Steinthorsdottir, M., Jardine, P. E., & Rember, W. C. (2021). Near-Future pCO_2 During the hot Miocene Climatic Optimum. *Paleoceanography and Paleoclimatology*, *36*(1), e2020PA003900. https://doi.org/10.1029/2020pa003900
Stinchcomb, G. E., Nordt, L. C., Driese, S. G., Lukens, W. E., Williamson, F. C., & Tubbs, J. D. (2016). A data-driven spline model designed to predict paleoclimate using paleosol geochemistry. *American Journal of Science*, *316*, 746–777. https://doi.org/10.2475/08.2016.02
Suarez, M. B., Passey, B. H., & Kaakinen, A. (2011). Paleosol carbonate multiple isotopologue signature of active East Asian summer monsoons during the late Miocene and Pliocene. *Geology*, *39*, 1151–1154. https://doi.org/10.1130/G32350.1
Sun, X., & Wang, P. (2005). How old is the Asian monsoon system? Palaeobotanical records from China. *Palaeogeography, Palaeoclimatology, Palaeoecology*, *222*, 181–222. https://doi.org/10.1016/j.palaeo.2005.03.005
Su, R., Sun, D., Chen, H., Chen, X., & Li, Z. (2010). Evolution of Asian monsoon variability revealed by oxygen isotopic record of middle Holocene massive coral in the northern South China Sea. *Quaternary International*, *213*, 56–68. https://doi.org/10.1016/j.quaint.2009.04.006
Tada, R., Zheng, H., & Clift, P. D. (2016). Evolution and variability of the Asian monsoon and its potential linkage with uplift of the Himalaya and Tibetan Plateau. *Progress in Earth and Planetary Science*, *3*(1), 1–26. https://doi.org/10.1186/s40645-016-0080-y
Tardif, D., Fluteau, F., Donnadieu, Y., Le Hir, G., Ladant, J.-B., Sepulchre, P., et al. (2020). The origin of Asian monsoons: A modelling perspective. *Climate of the Past*, *16*, 847–865. https://doi.org/10.5194/cp-16-847-2020

Utescher, T., Bruch, A. A., Erdei, B., François, L., Ivanov, D., Jacques, F. M. B., et al. (2014). The Coexistence Approach-Theoretical background and practical considerations of using plant fossils for climate quantification. *Palaeogeography, Palaeoclimatology, Palaeoecology*, *410*, 58–73. https://doi.org/10.1016/j.palaeo.2014.05.031

van der Boon, A., Beniest, A., Ciurej, A., Gaździcka, E., Grothe, A., Sachsenhofer, R. F., et al. (2018). The Eocene-Oligocene transition in the North Alpine Foreland Basin and subsequent closure of a Paratethys gateway. *Global and Planetary Change*, *162*, 101–119. https://doi.org/10.1016/j.gloplacha.2017.12.009

Wang, B., & LinHo, L. (2002). Rainy season of the Asian-Pacific summer monsoon. *Journal of Climate*, *15*, 386–398. https://doi.org/10.1175/1520-0442(2002)015<0386:rsotap>2.0.co;2

Wang, H., Lu, H., Zhao, L., Zhang, H., Lei, F., & Wang, Y. (2019). Asian monsoon rainfall variation during the Pliocene forced by global temperature change. *Nature Communications*, *10*, 1–8. https://doi.org/10.1038/s41467-019-13338-4

Wang, P. X., Wang, B., Cheng, H., Fasullo, J., Guo, Z., Kiefer, T., & Liu, Z. (2017). The global monsoon across time scales: Mechanisms and outstanding issues. *Earth-Science Reviews*, *174*, 84–121. https://doi.org/10.1016/j.earscirev.2017.07.006

Wang, W. M., Chen, G. J., & Liao, W. (2015). Oligocene palynoflora from Nanning Basin in Guangxi and its palaeoenvironmental significance. *Quaternary Sciences*, *35*, 1–10.

Wang, X., Carrapa, B., Sun, Y., Dettman, D. L., Chapman, J. B., Caves Rugenstein, J. K., et al. (2020). The role of the westerlies and orography in Asian hydroclimate since the late Oligocene. *Geology*, *48*, 728–732. https://doi.org/10.1130/G47400.1

Wu, L., Kravchinsky, V. A., & Potter, D. K. (2017). Apparent polar wander paths of the major Chinese blocks since the Late Paleozoic: Toward restoring the amalgamation history of east Eurasia. *Earth-Science Reviews*, *171*, 492–519.

Xie, Y., Wu, F., & Fang, X. (2019). Middle Eocene East Asian monsoon prevalence over southern China: Evidence from palynological records. *Global and Planetary Change*, *175*, 13–26. https://doi.org/10.1016/j.gloplacha.2019.01.019

Xie, Y., Wu, F., & Fang, X. (2020). A major environmental shift by the middle Eocene in southern China: Evidence from palynological records. *Review of Palaeobotany and Palynology*, *278*, 104226.

Yancheva, G., Nowaczyk, N. R., Mingram, J., Dulski, P., Schettler, G., Negendank, J. F. W., et al. (2007). Influence of the intertropical convergence zone on the East Asian monsoon. *Nature*, *445*, 74–77. https://doi.org/10.1038/nature05431

Yang, D., Uno, K. T., Souron, A., McGrath, K., Pubert, É., & Cerling, T. E. (2020). Intra-tooth stable isotope profiles in warthog canines and third molars: Implications for paleoenvironmental reconstructions. *Chemical Geology*, *554*, 119799. https://doi.org/10.1016/j.chemgeo.2020.119799

Ying, T., Shaw, D., & Schneider, S. (2018). Oligocene fossil assemblages from Lake Nanning (Yongning Formation; Nanning Basin, Guangxi Province, SE China): Biodiversity and evolutionary implications. *Palaeogeography, Palaeoclimatology, Palaeoecology*, *505*, 100–119. https://doi.org/10.1016/j.palaeo.2018.05.033

Zhao, R. (1993). Conclusion. *Vertebrata Palasiatica*, *31*, 183–187. https://doi.org/10.1007/978-3-322-95368-1_9

Zhisheng, A., Yongsong, H., Weiguo, L., Zhengtang, G., Clemens, S., Li, L., et al. (2005). Multiple expansions of C_4 plant biomass in East Asia since 7 Ma coupled with strengthened monsoon circulation. *Geology*, *33*, 705–708. https://doi.org/10.1130/G21423.1